arXiv:0905.1542v2 [quant-ph] 13 May 2009

Experimental demonstration of topological error correction

Wei-Bo Gao,[1] Austin G. Fowler,[2] Robert Raussendorf,[3] Xing-Can Yao,[1] He Lu,[1] Ping Xu,[1]
Chao-Yang Lu,[1] Cheng-Zhi Peng,[1] Youjin Deng,[1] Zeng-Bing Chen,[1] and Jian-Wei Pan[1, 4]

[1]Hefei National Laboratory for Physical Sciences at Microscale and Department of Modern Physics,
University of Science and Technology of China, Hefei, Anhui 230026, China
[2]Institute for Quantum Computing, University of Waterloo, Waterloo, ON, N2L 3G1, Canada
[3]Department of Physics and Astronomy, University of British Columbia, Vancouver, BC, V6T 1Z1, Canada
[4]Physikalisches Institut, Universität Heidelberg, Philosophenweg 12, 69120 Heidelberg, Germany

(Dated: May 13, 2009)

Abstract: Topological error correction–a novel method to actively correct errors based on cluster states with topological properties–has the highest order of tolerable error rates known to date ($\sim 10^{-2}$). Moreover, the scheme requires only nearest-neighbour interaction, particularly suitable for most physical systems. Here we report the first experimental demonstration of topological error correction with an 8-qubit optical cluster state. In the experiment, it is shown that a correlation can be protected against a single error on any single qubit. In addition, when all qubits are simultaneously subjected to errors with equal probability, the effective error rate is significantly reduced, clearly verifying the advantage of topological error correction. The quantum gate with the error rate below the threshold is within the current experimental technology. We believe topological error correction should be a critical ingredient for the future large-scale quantum computation.

I: INTRODUCTION

Quantum computers exploit the laws of quantum mechanics for computation, which results in quantum algorithms that can be exponentially more efficient than their classical counterparts. Given the ability to reliably manipulate a large number of quantum two-level systems called quantum bits (qubits), one could more efficiently factor integers [1], search an unsorted database [2] and simulate quantum physics [3, 4]. However, due to the degrading effects of decoherence, the high degree of quantum control required by quantum computation is notoriously hard to achieve in the laboratory. Two orthogonal paths have been proposed to address this problem, namely *quantum error correction* (QEC) [5, 6, 7] and *topological quantum computation* (TQC) [8, 9, 10].

The capstone result in QEC is the so-called threshold theorem [11, 12, 13, 14, 15]. It states that, as long as the error p per gate in a quantum computer is smaller than a threshold value p_c it is effectively as good as having no error at all. The price to pay is a poly-logarithmic, and thus acceptable, overhead in computational resources. Experimentally, some simple QEC codes have been demonstrated in nuclear magnetic resonance systems [16, 17] and ion traps [18]. Nevertheless, most methods of fault-tolerant quantum computing with high threshold ($10^{-4} - 10^{-2}$) [11, 12, 13, 14, 15] require strong long-range interaction, which is difficult to implement in most physical systems. In architectures with geometric constraints, and in particular, only nearest-neighbor interaction, fault-tolerance is much more difficult to achieve. A recent fault-tolerance threshold for a two-dimensional lattice of qubits with only local and nearest-neighbor gates is 1.9×10^{-5} [19].

TQC achieves fault-tolerance in a different way. In TQC, quantum information is encoded in non-local topological degrees of freedom which are largely, albeit not completely [20], immune to decoherence. Quantum gates are implemented by braiding low-energy effective particles called anyons [21]. The conceptual appeal of topological quantum computation is, at present, balanced by the difficulty of realizing it in the laboratory. An advanced physical system potentially suited for TQC is the two-dimensional electron gas in the fractional quantum Hall regime. Two recent experiments [22, 23] have demonstrated that low-energy quasi-particles in the $\nu = 5/2$ state are indeed of fractional charge $e/4$. Nevertheless, it still remains very challenging to experimentally manipulate anyons and verify their braiding properties.

Very recently, a novel scheme for fault-tolerance was proposed: *topological cluster state quantum computing* (TCQC) [24, 25]. It is based on three-dimensional (3D) cluster states with topological properties that enable both the computation and the topological error correction (TEC) [24, 25, 26]. TEC combines the advantages of QEC and TQC, that is, active error correction and topological properties similar to TQC. The protocol of TEC has several features: (i) 3D cluster states form an inherently error-robust “fabric” for computation. The same local measurements that drive the computation also yield the syndrome for error correction. (ii) The scheme has a high error threshold of 0.7%, leaving room for the unavoidable imperfections of realistic physical devices. (iii) The scheme is local in a 3D setting. Only nearest-neighbor and translation-invariant interaction is required, and thus TCQC is suitable to be realized in numerous systems, with two detailed architectures already proposed [27, 28]. (iv) the scheme can be mapped to a local setting in two spatial dimensions plus time [25].

In the present experiment, we exploit an optical 8-qubit cluster state to realize TEC, an essential ingredient in TCQC. While optical systems are leading the way [29, 30], the generation of cluster states with more than 6 qubits still remains challenging. In this work, we create an 8-qubit cluster state hyper-entangled [31] in the polarization and spatial modes. After creation of the cluster state, we measure its qubits locally, as required in TCQC. Error syndromes are then constructed from the measurement outcomes and one correlation is protected. We demonstrate: 1), if only one physical qubit suffers an error, the noisy qubit can be located and corrected, and 2), if all qubits are simultaneously subjected to errors with equal probability, the correlation protected with TEC has a lower error rate than without correction, and thus TEC is still superior.

II: CLUSTER STATES AND QUANTUM COMPUTING

In cluster state quantum computing [32], local projective measurements replace unitary evolution as the elementary process driving a quantum computation. The computation begins with a highly entangled multi-qubit state, the so-called cluster state. Any quantum algorithm can be performed on a (sufficiently large) cluster state. Quantum information is written into the cluster, processed and read out by one-qubit measurements only. A quantum algorithm is specified by the choice of local measurement bases for the cluster qubits. As the computation proceeds, the entanglement in the resource cluster state is progressively destroyed.

The computational resource, the cluster state $|G\rangle$ [33, 34], is specified by an interaction graph G. The name "interaction graph" derives from the fact that $|G\rangle$ can be created from a product state via the Ising interaction, with the edges in G specifying which pairs of qubits interact. Formally, $|G\rangle$ is specified by its stabilizer, i.e., a complete set of operators K_a of which it is the unique joint eigenstate, $K_a\,|G\rangle = |G\rangle$, $\forall a$, where

$$K_a = X_a \otimes_{b|(a,b)\in E(G)} Z_b,\ \forall\, a \in V(G). \qquad (1)$$

Therein, $V(G)$ and $E(G)$ are the vertex and edge sets of G, respectively; (a,b) refers to an edge in $E(G)$; and X_a, Z_b denote the usual Pauli bit-flip and phase-flip operators respectively, acting on qubit a and b.

Cluster states in $d \geq 2$ dimensions are universal resources for quantum computation. Furthermore, TEC capability arises for the $d \geq 3$ cluster state [24]. This capability is also found in Kitaev's toric codes [35] and color codes [36, 37]. The error correction procedures for fault-tolerant 3D cluster state computation [24] and for quantum memory with the toric code [26] are the same, and their performance is described by a spin model [26].

III: TOPOLOGICAL ERROR CORRECTION

The ability to perform TEC is built into a class of cluster states that can be associated with a geometrical structure—the so-called 3D cell complex $\mathcal{L}$ in topology [38]. A 3D cell complex $\mathcal{L}$ consists of volumes, faces, edges and sites, as well as a boundary map (∂) between them. The boundary map is geometrically clear: ∂[volume] = *sum* of surrounding faces, ∂[face] = *sum* of surrounding edges, and ∂[edge] = *sum* of endpoints, where all addition is mod 2. Consider Fig. 1a where the dashed lines form a cube, the definition of a cell complex becomes complete if one associates a volume with the cube and identifies: 1), ∂[volume] = *sum* of the 6 square faces, 2), ∂[face] = *sum* of the 4 surrounding edges, and 3), ∂[edge] = *sum* of the 2 endpoints. Note that the *closed* surface of the cube, composed of the 6 faces, does not have a boundary since each edge is counted twice.

A cluster state $|G\rangle$ is associated with a 3D cell complex $\mathcal{L}$ as follows: one qubit lives on each face f_i and each edge e_j of $\mathcal{L}$. The interaction graph $G_{\mathcal{L}}$ has the face qubit i and edge qubit j as its vertices, and a graph-edge between vertices i and j if and only if e_j belongs to the boundary of f_i. This is illustrated below by taking Fig. 1a as an example, to which an 18-qubit cluster state $|G_{18}\rangle$ is assigned. The 18 qubits are classified into two groups: on each of the 6 faces lives a face qubit, and at each mid-point of the 12 edges lies an edge qubit. Ising-like couplings are introduced between every face qubit and its surrounding 4 edge qubits; the resulting interaction graph $G_{\mathcal{L}}$ is shown by the solid lines in Fig. 1a. Accordingly, $|G_{18}\rangle$ has 6 stabilizers K_f of the form shown in Eq. (1), with $f = 1, \cdots, 6$ specifying the 6 faces. Multiplication of these 6 stabilizers leads to the cancellation of all Zs and thus $\langle X_1 X_2 \cdots X_6\rangle = 1$. Therefore, despite each individual measurement X on the face qubits being randomly ± 1, the product of the 6 outcomes will be $+1$.

A much larger cell complex is needed for practical purposes; Fig. 1b displays a cell complex of $5 \times 5 \times T$ cells. The length T is frequently identified as a span of simulated time t. It can be shown that the tensor product of X of all face qubits on *any closed* surface F has unit expectation value. In other words, the cell complex has topological quantum correlation $C_F :\equiv \langle \otimes_{f\in F} X_f \rangle_F = 1$. A large cell complex has many closed surfaces F and thus many correlations C_F. These correlations enable computation as well as TEC. A brief and phenomenological explanation is given below.

For computation, a "defect" along the t direction is

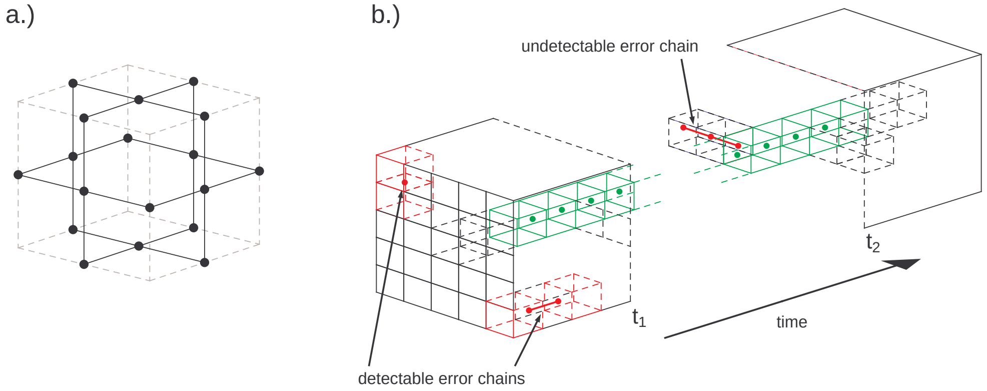

FIG. 1: Topological cluster states. **a**. An elementary lattice cell. Dashed lines represent the edges of the associated cell complex, while solid lines specify the interaction graph. Qubits, displayed as dots "•", are located on the faces and the edges of the elementary cell. **b**. A large topological cluster state of 5×5×T cells. All lines represent edges (1-cells) of the associated cell complex. Green dots represent local Z measurements, effectively removing these qubits from the cluster and thereby creating a non-trivial topology capable of supporting a single logical qubit. Red dots represent Z errors. Red cells indicate $C_{F_S} = -1$ at the ends of error chains. One axis of the cluster can be regarded as simulating "circuit time". The evolution of logical states from t_1 to t_2 is achieved by performing local X measurements on proper qubits between t_1 and t_2.

carved out through the 3D cell complex by performing local Z measurements. Such a defect is shown as the line of green dots in Fig. 1b. A logical qubit propagating forward in (simulated) time is then associated with two defects or with a defect and a boundary; see Fig. 1b for the latter. The initial preparation, the evolution, and the measurement of a single logical qubit are discussed in detail in ref. [39]. A quantum circuit (algorithm) is realized by appropriate braiding-like manipulation of defects (a schematic for the logical CNOT gate is shown in Fig. 7 in the Appendix).

We emphasize two points here. (1) The evolution of logical states from t_1 to t_2 is achieved by performing local X measurements on properly selected physical qubits between t_1 and t_2. (2) To enable quantum computation, we need to have *the topological quantum correlation* $C_{F_D} = 1$ on closed surfaces F_D enclosing defects. It is therefore crucial to protect $C_{F_\mathrm{D}} = 1$ in computation. In reality, errors can occur, and thus error correction is required.

The TEC capability follows automatically for a cluster state as long as it can be associated with a 3D cell complex. A closed surface F exhibits topological correlation $C_F = 1$ in the absence of errors, and thus the occurrence of negative correlation on F would imply one or more Z errors (a Z error immediately before measurement flips the X outcome). Besides the defect-enclosing surfaces F_D that carry quantum information, a large 3D cell complex contains many other closed surfaces F_S which enclose no defect. Measurements of topological correlations C_{F_S} yields a large amount of "redundant" information, which can be used as syndromes for error correction. Indeed, it has been shown [24] that, based on the syndromes collected from all elementary cells, errors can be correctly identified with high probability. The essential topological feature of this error correction is $\mathbb{Z}_2$-homology (See Appendix).

We conclude this section with a comment on the error model. First, as a measurement-based quantum computation, corrections suggested by the TEC protocol are not applied to the remaining cluster state but rather the classical measurement outcomes of X measurements. Next, in TEC it is sufficient to deal with Z errors, because: 1), X errors immediately before X measurements have no effect, and 2), an X error during preparation of the cluster state is equivalent to multiple Z errors.

IV: SIMPLER TOPOLOGICAL CLUSTER STATE

The cell complex in Fig. 1b protects one correlation $C_{F_D} = 1$ against a local Z error. Unfortunately, it contains 180 physical qubits per layer, significantly beyond the reach of available techniques. We shall design a simpler graph state $|G_8\rangle$ (shown in Fig. 2a) which mimics the cell complex in Fig. 1b. Despite having only 8 qubits in total, the cluster state $|G_8\rangle$ can be associated with a 3D nontrivial cell complex and it therefore possesses the TEC capability. While still too simple to perform nontrivial computation, $|G_8\rangle$ can be used to demonstrate TEC.

The 3D cell complex for state $|G_8\rangle$, denoted as $\mathcal{L}_8$, is displayed in Fig. 2b. It consists of 4 elementary volumes $\{v, w, y, z\}$, 6 faces $\{f_1, f_3, f_4, f_{1'}, f_{3'}, f_{4'}\}$, 2 edges $\{e_2, e_{2'}\}$, and 2 sites $\{s, t\}$. Accordingly, $|G_8\rangle$ has 6 face qubits and 2 edge qubits.

All 6 faces have the same boundary—the sum of edges e_2 and $e_{2'}$, and thus the sum of any two of these faces

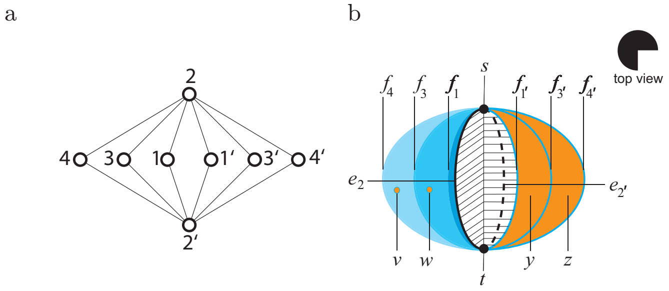

FIG. 2: Cluster state $|G_8\rangle$ and its cell complex $\mathcal{L}_8$. (a) Interaction graph G_8 of $|G_8\rangle$. (b) The corresponding three-dimensional cell complex $\mathcal{L}_8$, with volumes v, w, y, z, faces $f_1, f_3, f_4, f_{1'}, f_{3'}, f_{4'}$, edges $e_2, e_{2'}$ and sites s, t. The exterior and the volume element in the center are not in the complex. For better illustration, the cell complex is cut open and the front right quarter is removed, c.f. "top view".

Z_{error}	C_{13}	C_{34}	$C_{1'3'}$	$C_{3'4'}$	Z_{error}	C_{13}	C_{34}	$C_{1'3'}$	$C_{3'4'}$
1	-1	1	1	1	1′	1	1	-1	1
3	-1	-1	1	1	3′	1	1	-1	-1
4	1	-1	1	1	4′	1	1	1	-1

TABLE I: Location of a Z error in $|G_8\rangle$ and the syndromes $C_{13} = \langle X_1 X_3\rangle$ etc.

forms a closed surface F. The center volume of the cell complex $\mathcal{L}_8$ in Fig. 2b is carved out to mimic the defect in Fig. 1b, and the defect-enclosing topological correlation C_{F_D} is

$$C_{F_D} :\equiv \langle X_1 X_{1'}\rangle = 1. \tag{2}$$

To protect this computation-oriented correlation C_{F_D}, one makes use of the closed surfaces $f_4 \cup f_3$, $f_3 \cup f_1$, $f_{1'} \cup f_{3'}$, and $f_{3'} \cup f_{4'}$. These surfaces are the boundary of volumes v, w, y, z, respectively. The corresponding topological correlations

$$\langle X_1 X_3\rangle = \langle X_3 X_4\rangle = \langle X_{3'} X_{1'}\rangle = \langle X_{4'} X_{3'}\rangle = 1 \tag{3}$$

are used as syndromes for TEC. We can also directly calculate Eqs. (2) and (3) from inspecting the stabilizers of $|G_8\rangle$.

With the topological information in Eq. (3), the cluster state $|G_8\rangle$ is now robust against a single Z error—any Z error on physical qubits $1, 3, 4, 1', 3'$ and $4'$ can be located and corrected afterwards (see Table I).

V: PREPARATION OF THE 8-QUBIT CLUSTER STATE

In our experiment, the desired 8-qubit cluster state is created using spontaneous parametric down-conversion and linear optical elements. An ultraviolet mode-locked laser pulse passes through two β-barium borate (BBO) crystals which generate two pairs of highly entangled photons in the state $|\phi\rangle = (|H\rangle|H\rangle + |V\rangle|V\rangle)/\sqrt{2}$ in path 1-2 and 3-4 (See Fig. 3), where $|H\rangle$ ($|V\rangle$) denotes the horizontally (vertically) polarized photon. The photon pairs have an average two-fold coincidence count of about $2.4{\times}10^4 s^{-1}$ and a visibility of 92% (90%) in the H/V $(+/-)$ basis, where $|\pm\rangle = \frac{1}{\sqrt{2}}(|H\rangle \pm |V\rangle)$. The photons from path 2 and 3 are then combined at a polarizing beam-splitter (PBS) which transmits H and reflects V polarization. To ensure good spatial and temporal overlap, the photons are spectrally filtered ($\Delta\lambda_{\text{FWHW}} = 3.2\,\text{nm}$) and coupled by single-mode fibers. When four photons are emitted out of the output ports simultaneously, one can check that they are in the Greenberg-Horne-Zeilinger (GHZ) state

$$|\phi\rangle = (|H\rangle^{\otimes 4}_{1,2,3,4} + |V\rangle^{\otimes 4}_{1,2,3,4})/\sqrt{2}. \tag{4}$$

After photon 2 undergoes a Hadamard transformation, the state is converted to $(|H\rangle^{\otimes 3}_{1,3,4}|+\rangle_2 + |V\rangle^{\otimes 3}_{1,3,4}|-\rangle_2)/\sqrt{2}$.

Next, each photon passes through a PBS, and is then characterized by two spatial modes H' and V' as well as its polarization H and V. This can be seen as a process of redundant encoding ($\alpha|H\rangle + \beta|V\rangle \rightarrow \alpha|H\rangle|H'\rangle + \beta|V\rangle|V'\rangle$), effectively adhering a spatial qubit onto the polarization qubit. Thus we end up with an entangled 8-qubit cluster state:

$$\begin{aligned}|\psi\rangle &= \frac{1}{2}[|H\rangle^{\otimes 3}_{1,3,4}|H'\rangle^{\otimes 3}_{1',3',4'}(|HH'\rangle_{22'} + |VV'\rangle_{22'}) + \\ &\quad |V\rangle^{\otimes 3}_{1,3,4}|V'\rangle^{\otimes 3}_{1',3',4'}(|HH'\rangle_{22'} - |VV'\rangle_{22'})]\,. \end{aligned} \tag{5}$$

This is exactly the cluster state shown in Fig. 2b under Hadamard operations $H^{\otimes 8}$ on all qubits.

The measurement of the spatial qubits of this cluster state employs an optical interferometer combing the two paths onto a non-polarizing beam splitter with adjustable phase delay between these two paths. After this interferometer, the polarization information is then read out by placing a combination of a quarter-wave plate (QWP), a half-wave plate (HWP) and a PBS in front of the single-photon detectors. In our experiment, Sagnac-ring interferometers are constructed to achieve the required stability [40, 41] (See Fig. 3b(b)).

To characterize the cluster state, we use the method of entanglement witnesses to determine its state fidelity and detect the presence of genuine multi-particle entanglement (See Appendix). The fidelity, a measure of to what extent the desired state is created, is judged by the overlap of the experimentally produced state with the ideal one. We consider a special observable, which allows for lower bounds on the fidelity and is easily measurable with few correlation measurements. By making

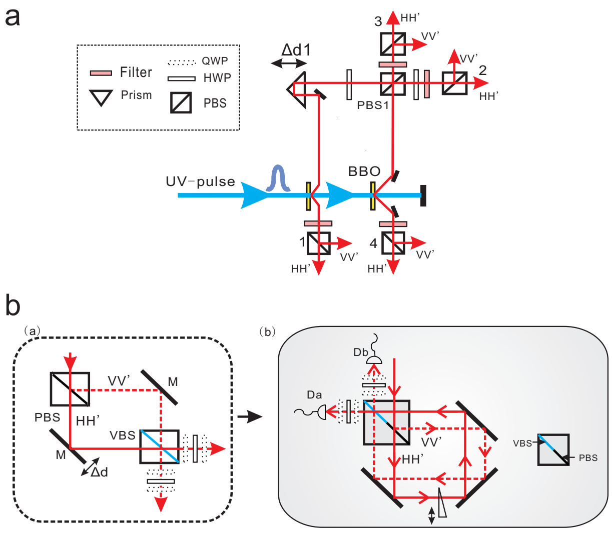

FIG. 3: Experimental setup for the generation of the 8-qubit cluster state and demonstration of topological error correction. **a**. An ultraviolet laser pulse passes through two nonlinear crystals (BBO), which are aligned to produce entangled photon pairs $|\phi\rangle$ in paths 1-2 and 3-4. By combining photons from paths 2 and 3 at polarizing beam-splitter (PBS) 1 and exploiting another four PBSs in output modes, the 8-qubit state $|\psi\rangle$ can be prepared. Prism $\Delta d1$ is used to ensure that the input photons arrive at the PBSs at the same time. Furthermore, every output is spectrally filtered ($\Delta\lambda_{FWHM} = 3.2$ nm) to ensure good temporal overlap. **b**(**a**). In order to engineer the noisy channels, the two output modes of a PBS are interacted at a beam splitter with a variable reflection beam-splitter (VBS) and then pass through a series of wave plates. **b**(**b**). The configuration of ultra-stable Sagnac-ring interferometers. The specially designed beam-splitter cubes are half PBS-coated and half VBS-coated. When the reflection of the VBS is adjusted to 1/2, we use it to characterize our prepared state. We insert high-precision small-angle prisms to satisfy fine adjustments of the relatively delay of the two different paths. These Sagnac-ring interferometers can be stable for up to ten hours.

these measurements, we estimate the fidelity of the created cluster state to be at least 0.73 ± 0.02. The notion of genuine multipartite entanglement characterizes whether generation of the state requires interaction of all parties, distinguishing the experimentally produced state from any incompletely entangled state. For the graph states, it is sufficient to prove the presence of genuine multipartite entanglement if their fidelities exceed the threshold of 0.5 [42]. Thus, with high statistical significance, the genuine 8-qubit entanglement of the cluster state created in our experiment is confirmed.

VI: EXPERIMENTAL TOPOLOGICAL ERROR CORRECTION

Given such a cluster state, error correction is implemented using a series of single-qubit measurements and classical correction operations. In the laboratory, operations are performed on state (5), which differs from $|G_8\rangle$ in Fig. 1b by a Hadamard operation $H^{\otimes 8}$. Therefore, the to-be-protected correlation $X_1X_{1'}$ in Eq. (2) corresponds to $Z_1Z_{1'}$ in the experiment; the same applies to the syndrome correlations (3). Similarly, X errors are engineered instead of Z errors.

In the experiment, the noisy quantum channels on polarization qubits are engineered by one HWP sandwiched with two quarter-wave plates (QWPs), which are set at 90 degrees. By randomly setting the HWP axis to be oriented at θ with respect to the horizontal direction, the noisy quantum channel can be engineered with a bit-flip error probability of $p = \sin^2(2\theta)$. Concerning the spatial qubits, the noisy quantum channels are engineered by interacting two spatial modes at a beam splitter with a variable reflection probability R ($R \in [0, 1]$). The beam splitter is specially coated such that the reflection probability will change from 0 to 1 when it is moved vertically to the optical stage.

By varying variables θ and R, we first study the case that at most one of the 6 qubits $1, 1', 3, 3', 4, 4'$ undergoes an X error. The syndrome correlations are measured, and the results are shown in Fig. 4. By comparing our experimental outcomes with the theoretical predictions in Table I (shown as grey bars in Fig. 4), one is indeed able to precisely locate the physical qubit undergoing an X error.

We then consider the case of more than one physical qubit being subjected to errors, but with only the preservation of the $Z_1Z_{1'}$ correlation determining success. When each physical qubit suffers from errors with an equal probability $0 < p < 1$, the error rate of $Z_1Z_{1'}$ without error correction is $P = 1 - (1-p)^2 - p^2$. With error correction, the residual error is

$$\begin{aligned} P = 1 \; & - \; [(1-p)^6 + p^6] - [6p(1-p)^5 + 6(1-p)p^5] \\ & - \; [9p^2(1-p)^4 + 9p^4(1-p)^2]. \end{aligned} \tag{6}$$

The two respective curves P vs. p are plotted in Fig. 5. For small error rate p, the residual error rate after error correction is significantly reduced as compared to the unprotected case. As demonstrated in Fig. 5, our experimental results are in good agreement with these theoretical predictions. Considerable improvement of the robustness of the $Z_1Z_{1'}$ correlation can be seen both in theory and in practice.

The imperfections in the experiment are mainly caused by three effects. First, the undesired components in the H/V basis are generated by high-order emissions of entangled photons. Second, photon overlapping at the po-

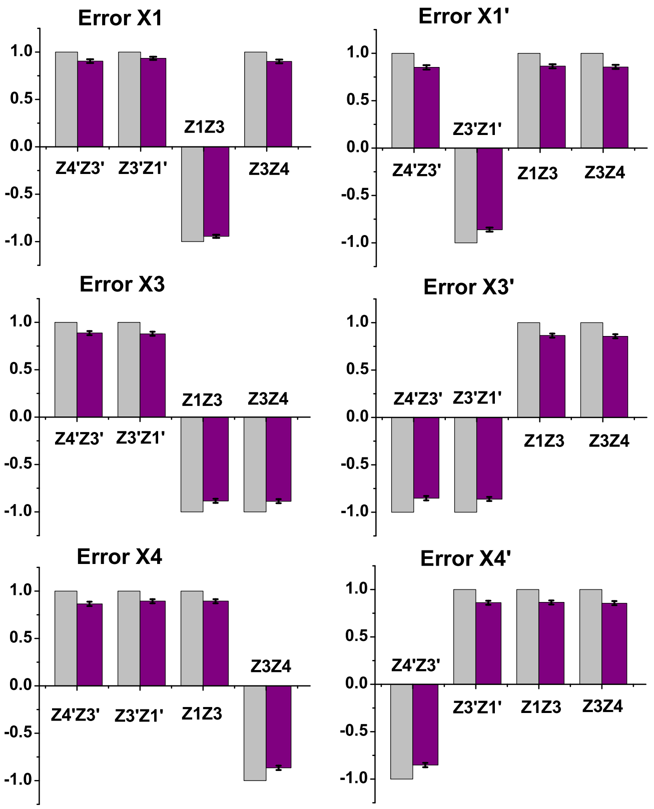

FIG. 4: Experimental results of syndrome values of error correction. Only one qubit is subjected to errors in each subfigure. The grey columns show the theoretical values of syndrome values while the purple columns show the experimental values. The error bars represent one standard deviation, deduced from propagated Poissonian counting statistics of the raw detection events.

larizing beam splitters is imperfect. Third, the engineering of artificial errors is not precise. In spite of these imperfections, the advantage of topological error correction is clearly verified in the experiment.

VII: DISCUSSION

In the current work, we have experimentally demonstrated topological error correction with an 8-qubit photonic cluster state. This state represents the current state-of-the-art for preparation of cluster states in any qubit system and is of particular interest in studying multipartite entanglement and quantum information processing. The scalable construction of cluster states in the future will require further development of high-efficiency entanglement sources and single-photon detectors [43]. Recent results have shown that if the product of the number resolving detector efficiency and the source efficiency is greater than 2/3, then efficient linear optical quantum computation is possible [44]. Solid technical progress towards this goal has been made such as single-photon sources with quantum memory [45] and photon-number-resolving detectors [46].

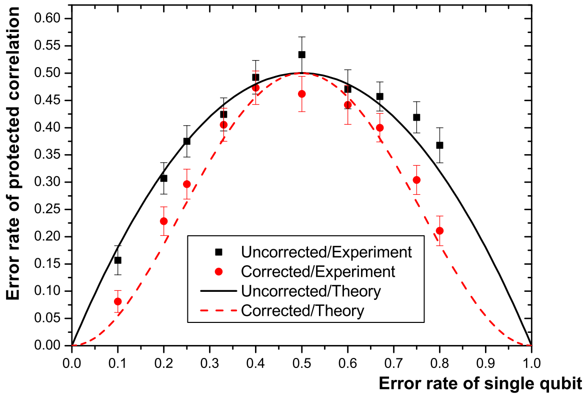

FIG. 5: Results of error correction. The logical error rate is given before and after error correction when each physical qubit suffers from an equal error rate ranging from 0 to 1. Black square dots and red round dots represent experimental values of the protected correlation before and after error correction, respectively. The black solid line represents the theoretical uncorrected error rate of the protected correlation, while the red dashed line represents the corrected error rate shown in Eq. (6). The experimental data is consistent with the theoretical prediction and the advantage of error correction is clearly demonstrated.

The current work represents the first experimental demonstration of topological error correction. Given sufficient qubits and physical error rates below 0.7%, arbitrary quantum computations could be performed arbitrarily reliably. The high threshold error rate is especially remarkable given only nearest neighbor-interactions are required. These features make topological error correction especially well-suited to physical systems geometrically constrained to nearest-neighbor interactions, such as quantum dots [47], Josephson junction qubits [48], ion traps [49], cold atoms in optical lattices [50] and photonic modules [28]. Especially, the quantum gate with the error rate below the threshold required in TEC is within the reach of the current experimental technology [51]. It would be interesting in future work to exploit cluster states of reachable size to implement topologically error-protected quantum algorithms by measurements.

APPENDIX I: TOPOLOGICAL CLUSTER STATE QUANTUM COMPUTATION

Cluster states and homology. The topological feature of error-correction with three-dimensional (3D) cluster states is homology, which we shall illustrate in 2D for simplicity. Displayed in Fig. 6 is a 2D plane with two point defects (●). The boundary of a surface is defined as the *sum* of all the surrounding chains. For instance, the boundary of the surface f (shown in blue) is the sum of e_1 and e_2, denoted as $\partial f = e_1 \cup e_2$. Because of the presence of the point defects, each of the three chains, e_1, e_2, and e_3, is not sufficient to be the whole boundary of a surface. Analogously, the boundary of a chain is defined as the sum of its endpoints. Since the three chains are cycles, they have no boundary—i.e, $\partial e_1 = \partial e_2 = \partial e_3 = 0$. The chain e_2 can be smoothly transformed into e_1, and vice versa. In other words, e_1 and e_2 differ only by the boundary of a surface: $e_2 = e_1 + \partial f$. We say that e_1 and e_2 are homologically equivalent. In contrast, e_3 is inequivalent to e_1 or e_2 due to the right-hand-side defect. The homology in higher dimensions is defined in an analogous way. In 3D, the boundary of a volume is the sum of all its surrounding surfaces. A closed surface F is said to have no boundary—$\partial F = 0$; a simple example is the surface of a sphere. Two surfaces F and F' are homologically equivalent if they differ only by the boundary of a volume V: $F' = F \pm \partial V$.

In topological cluster state computation, the error correction scheme only involves local measurements in the X basis, with outcomes $\lambda = \pm 1$. Computational results are represented by correlations $R(F) = \prod_{a \in F} \lambda_a$ of these outcomes on a closed surface F—$\partial F = 0$. As in any encoding, error-resilience is brought about by redundancy. A given bit of the computational result is inferred not only from a particular surface F, but from any one in a huge homology equivalence class. This is because two homologically equivalent surfaces F and F' have the same correlation $R(F) = R(F')$ in the absence of errors [24]. As a result, one has $R(\partial V) = 1$ for every volume V. An outcome of -1 then indicates the occurrence of an error in the volume V, and thus $R(\partial V)$ can be used as error syndrome. We obtain one bit of such error syndrome per lattice cell; c.f. Fig. 1a.

The errors have a geometrical interpretation: they correspond to chains e. Again, homology becomes relevant: Two homologically equivalent error chains e and e' have the same effect on computation.

In TEC with cluster states, the computational results and the syndromes are contained in correlations among outcomes of local X-measurements. Detecting and correcting only phase flips of physical qubits is thus sufficient to correct arbitrary errors. Nevertheless, both bit flip and phase flip errors are present at the level of logical operations. The qubits in a 3D cluster state live on the faces and edges of the associated lattice. Logical phase errors are caused by erroneous measurement of face qubits, and logical spin flip errors are by erroneous measurement of edge qubits. For example, the 8-qubit cluster state $|G_8\rangle$ considered in this experiment has, in addition to the correlations (3), the correlation $\langle G_8 | X_2 \otimes X_{2'} | G_8 \rangle = 1$. It can be derived from a dual complex [24], and provides one bit of (dual) syndrome for the edge qubits of $\mathcal{L}_8$.

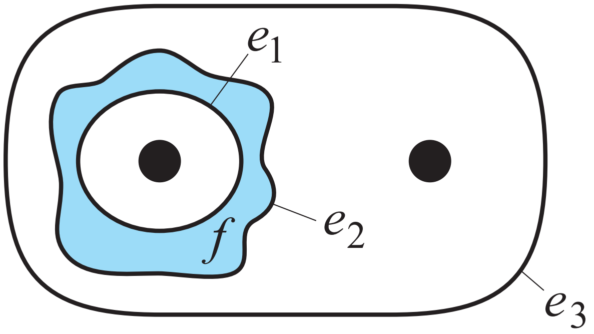

FIG. 6: Illustration of homological equivalence in two dimensions. Here is a 2D plane with two point defects (●). All three chains, e_1, e_2, and e_3, are cycles and thus have no boundary. They are furthermore nontrivial: each of them is insufficient to be the whole boundary of a surface. The cycles e_1 and e_2 are said to be homologically equivalent because they differ only by the boundary ∂f of the surface f. In contrast, e_3 is not equivalent to e_1 or e_2. In other words, e_1 and e_2 can collapse into each other by *smooth* deformation, while e_3 cannot be smoothly transformed into e_2 or e_1 because of the presence of the right-hand-side defect. In the topological cluster state quantum computation, errors are represented by chains. two homologically equivalent error chains have the same effect on computation.

Topologically protected quantum gates are performed by measuring some regions of qubits in the Z basis, which effectively removes them. The remaining cluster, whose qubits are to be measured in the X and $X \pm Y$ basis, thereby attains a non-trivial topology in which fault-tolerant quantum gates can be encoded. Fig. 7 shows a macroscopic view of a 3D sub-cluster for the realization of a topologically protected CNOT gate [25, 52]. Only the topology of the cluster matters, individual lattice cells are not resolved. The cluster qubits in the line-like regions D are measured in the Z-basis, the remaining cluster qubits in the X-basis.

The fault-tolerance of measurement-based quantum computation with a 3D cluster state can be understood by mapping it to a Kitaev surface code propagating in time [25]. In this picture, a 3D cluster state consists of many linked toric code surfaces plus extra qubits for code stabilizer measurement, entangled with these surfaces. The local measurements in each slice have the effect of teleporting the encoded state to the subsequent code surface. The code surfaces can support many encoded qubits because they have boundary. Encoded gates are implemented by changing the boundary conditions with time. This process is illustrated in Fig. 7 for the CNOT gate. Pieces of boundary in the code surface are created by the intersection of the line-like regions D with surfaces of "constant time". The 1-chains displayed in red represent encoded Pauli operators $\overline{X}$ at a given instant of simulated time. When propagating forward, an initial

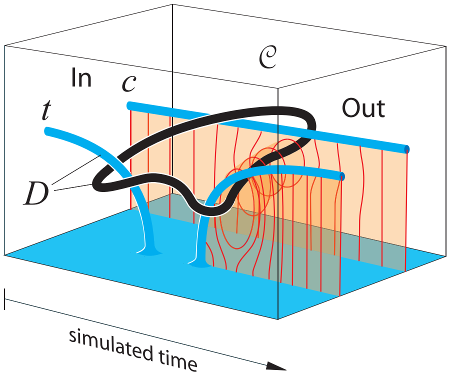

FIG. 7: Topological gates with 3D cluster states. The sub-cluster $\mathcal{C}$ (indicated by the wire frame) realizes an encoded CNOT gate between control c and target t. The regions D are missing from the cluster. Each line-like such region supports the world-line of one encoded qubit. One of the four homologically non-trivial correlation surfaces for the encoded CNOT is shown in orange.

operator $\overline{X}_c$ is converted into $\overline{X}_c \otimes \overline{X}_t$ as required by conjugation under CNOT.

Further Reading. For the interested reader we add a few references. The topological error-correction capability in 3D cluster states is, for the purpose of establishing long-range entanglement in the presence of noise, discussed in [24]. How to perform universal fault-tolerant quantum computation with 3D cluster states is described in [24] and in terms of stabilizers in [39]. In [25], a mapping from three spatial dimensions to two spatial dimensions plus time is provided, and the fault-tolerance threshold is improved to 0.7%, for both the three and the two-dimensional version. The 2D scheme is described solely in terms of the toric code in [54].

APPENDIX II: CHARACTERIZATION OF THE 8-QUBIT CLUSTER STATE

In order to characterize the generated 8-qubit cluster state, we use entanglement witnesses to verify its genuine multipartite entanglement [55]. If $\mathcal{W}$ is an observable which has a positive expectation value on all biseparable states and a negative expectation value on the generated entangled state, we call this observable an entanglement witness. With the method introduced in Ref. [56], the witness is constructed as

$$\mathcal{W}=\frac{1}{2}-|\psi\rangle\langle\psi|+|\psi'\rangle\langle\psi'|, \qquad (7)$$

where

$$\begin{aligned}|\psi'\rangle=\frac{1}{2}[&|H\rangle^{\otimes 3}_{1,3,4}|H'\rangle^{\otimes 3}_{1',3',4'}(|HH'\rangle_{22'}+|VV'\rangle_{22'})\\ &-|V\rangle^{\otimes 3}_{1,3,4}|V'\rangle^{\otimes 3}_{1',3',4'}(|HH'\rangle_{22'}-|VV'\rangle_{22'})]. \qquad (8)\end{aligned}$$

After decomposing the witness into a number of local von Neumann (or projective) measurements, we obtain

$$\begin{aligned}\mathcal{W}=\frac{1}{2}-\frac{1}{4}[-\{\frac{1}{8}\sum_{k=0}^{7}M_k\}+\{X_2X_{2'}\frac{1}{8}\sum_{k=0}^{7}M_kX_2X_{2'}\}\\ +\{(\frac{1}{6}\sum_{k=0}^{5}N_k)(|HH'\rangle\langle HH'|-|VV'\rangle\langle VV'|)_{22'}\}], \quad (9)\end{aligned}$$

where

$$\begin{aligned}M_k &= (-1)^k[\cos(\frac{k\pi}{8})X+\sin(\frac{k\pi}{8})Y]^{\otimes 8},\\ N_k &= (-1)^k[\cos(\frac{k\pi}{6})X+\sin(\frac{k\pi}{6})Y]^{\otimes 6}_{1,3,4,1',3',4'} \quad (10)\end{aligned}$$

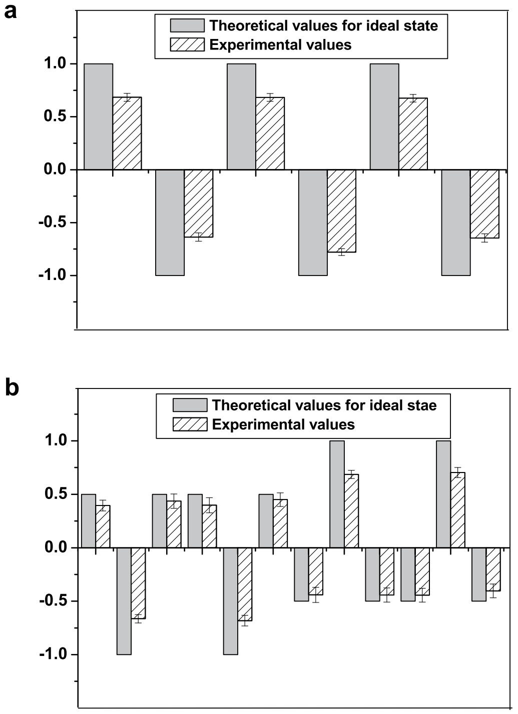

FIG. 8: The experimental characterization of the 8-qubit cluster state. **a**. The expectation values of $N_k(|HH'\rangle\langle HH'|-|VV'\rangle\langle VV'|)_{22'}$, each derived from 8-qubit coincidence events collected in 4 mins. **b**. The expectation values of M_k and $X_2X_{2'}M_kX_2X_{2'}$ $(k \in 1,2,3,5,6,7)$, each also derived from the data in 4 mins. They are sufficient to calculate the value of the witness in Eq. 9. The error bars represent one standard deviation, deduced from propagated Poissonian counting statistics of the raw detection events.

The experimental results have been depicted in Fig. 8, from which we obtain $\langle\mathcal{W}\rangle < -0.23 \pm 0.02$, thus having 11.5 standard deviations and verifying genuine multipartite entanglement in the generated state. In addition, the experimental fidelity of the state $F=\langle\psi|\rho_{\text{exp}}|\psi\rangle$ can be estimated from the inequality $F > 1/2 - \mathcal{W}$. We can thus calculate the state fidelity $F > 0.73 \pm 0.02$.

Acknowledgements We acknowledge insightful discussions with M. A. Martin-Delgado, O. Gühne. This work has been supported by the NNSF of China, the CAS, and the National Fundamental Research Program (under Grant No. 2006CB921900).

[1] P. W. Shor, In *Proc. 35th Annual Symposium on Foundations of Computer Science* (IEEE, New York, 1994), pp. 124-134.
[2] L. K. Grover, Phys. Rev. Lett. **79**, 325 (1997).
[3] R. P. Feynman, Int. J. Theor. Phys. **21**, 467 (1982).
[4] S. Lloyd, Science **273**, 1073 (1996).
[5] A. R. Calderbank, P. W. Shor, Phys. Rev. A **54**, 1098 (1996).
[6] A. M. Steane, Proc. R. Soc. Lond. A**425**, 2551 (1996).
[7] D. Gottesman, Phys. Rev. A **57**, 127 (1998).
[8] M. H. Freedman, M. Larsen, Z. Wang, Commun. Math. Phys. **227**, 605 (2002).
[9] N. E. Bonesteel *et al.*, Phys. Rev. Lett. **95**, 140503 (2005).
[10] P. Bonderson, M. H. Freedman, C. Nayak, Phys. Rev. Lett. **101**, 010501 (2008).
[11] E. Knill, R. Laflamme, W. H. Zurek, (quant-ph/9610011) (1996).
[12] D. Aharonov, M. Ben-Or, Proc. ACM STOC **29**, 176 (1997).
[13] A. Yu. Kitaev, Russ. Math. Surv. **52**, 1191 (1997).
[14] E. Knill, Nature **434**, 39 (2005).
[15] P. Aliferis, D. Gottesman, J. Preskill, Quant. Inf. Comput. **6**, 97 (2006).
[16] D. G. Cory *et al.*, Phys. Rev. Lett. **81**, 2152 (1998).
[17] E. Knill, R. Laflamme, R. Martinez, C. Negrevergne, Phys. Rev. Lett. **86**, 5811 (2001).
[18] J. Chiaverini *et al.*, Nature **432**, 602 (2004).
[19] K. M. Svore, D. P. DiVincenzo, B. M. Terhal, Quant. Inf. Comput.**7**, 297 (2007).
[20] C. Nayak *et al.*, Rev. Mod. Phys. **80**, 1083 (2008).
[21] F. Wilczek, Fractional Statistics and Anyon Superconductivity (World Scientific Press, Singapore, 1990).
[22] M. Dolev *et al.*, Nature **452**, 829 (2008).
[23] P. I. Radu *et al.*, Science **320**, 899 (2008).
[24] R. Raussendorf, J. Harrington, K. Goyal, Ann. Phys. **321**, 2242 (2006).
[25] R. Raussendorf, J. Harrington, Phys. Rev. Lett. **98**, 190504 (2007).
[26] E. Dennis, A. Landahl, A. Yu. Kitaev, J. Preskill, J. Math. Phys. **43**, 4452 (2002).
[27] R. Stock, D. F. V. James, (quant-ph/0808.1591) (2008).
[28] S. J. Devitt *et al.*, (quant-ph/0808.1782) (2008).
[29] P. Walther *et al.*, Nature **434**, 169 (2005).
[30] C. Y. Lu *et al.*, Nature Physics **3**, 91 (2007).
[31] P. G. Kwiat, J. Mod. Opt. **44**, 2173 (1997).
[32] R. Raussendorf, H. J. Briegel, Phys. Rev. Lett. **86**, 5188 (2001).
[33] H. J. Briegel, R. Raussendorf, Phys. Rev. Lett. **86**, 910 (2001).
[34] D. Schlingemann, R. F. Werner, Phys. Rev. A **65**, 012308 (2002).
[35] A. Yu. Kitaev, Ann. Phys. **303**, 2 (2003).
[36] H. Bombin and M. A. Martin-Delgado, Phys. Rev. Lett. **97**, 180501 (2006).
[37] H. Bombin and M. A. Martin-Delgado, Phys. Rev. Lett. **98**, 160502 (2007).
[38] A. Hatcher, Algebraic Topology. (Cambridge Univ. Press, Cambridge, 2002).
[39] A. G. Fowler, K. Goyal, (quant-ph/0805.3202) (2008).
[40] T. Nagata *et al.*, Science **316**, 726 (2007).
[41] M. P. Almeida *et al.*, Science **316**, 579 (2007).
[42] G. Tóth, O. Gühne, Phys. Rev. Lett. **94**, 060501 (2005).
[43] J. L. O'Brien, Science **318**, 1567 (2007).
[44] M. Varnava, D. E. Browne, T. Rudolph, Phys. Rev. Lett. **100**, 060502 (2008).
[45] S. Chen *et al.*, Phys. Rev. Lett. **97**, 173004 (2006).
[46] B. E. Kardynal, Z. L. Yuan, A. J. Shields, Nature Physics **2**, 425 (2008).
[47] D. Press *et al.*, Nature **456**, 218 (2008).
[48] T. Hime *et al.*, Science **314**, 1427 (2006).
[49] W. K. Hensinger *et al.*, Appl. Phys. Lett. **88**, 034101 (2006).
[50] D. Jaksch *et al.*, Phys. Rev. Lett. **82**, 1975 (1999).
[51] J. Benhelm, *et al.*, Nature physics **4**, 463-466 (2008).
[52] R. Raussendorf, J. Harrington, K. Goyal, New J. Phys. **9**, 199 (2007).
[53] R. Raussendorf, S. Bravyi, J. Harrington, Phys. Rev. A **71**, 062313 (2005).
[54] A. G. Fowler, A. M. Stephens, P. Groszkowski, (quant-ph/0803.0272) (2008).
[55] M. Bourennane *et al.*, Phys. Rev. Lett. **92**, 087902 (2004).
[56] O. Gühne, C. Y. Lu, W. B. Gao, J. W. Pan, Phys. Rev. A **76**, 030305 (2007).